crystals

MDPI

Article

Hydrothermal Synthesis of ZnO Nanoflowers: Exploring the Relationship between Morphology, Defects, and Photocatalytic Activity

Essam M. Abdel-Fattah [1,2,*], Salman M. Alshehri [1], Satam Alotibi [1], Mohammed Alyami [1] and Doaa Abdelhameed [1,2]

[1] Department of Physics, College of Science and Humanities, Prince Sattam Bin Abdulaziz University, P.O. Box 173, Al-Kharj 11942, Saudi Arabia
[2] Physics Department, Faculty of Science, Zagazig University, Zagazig 44519, Egypt
* Correspondence: e.abdelfattah@psau.edu.sa

Abstract: Two forms of flower-like ZnO nanostructures were synthesized using hydrothermal methods at various growth times/temperatures and zinc precursors. The morphology, structure, chemical composition, and optical properties of these ZnO nanoflowers were studied using a scanning electron microscope (SEM), X-ray diffraction spectroscopy (XRD), X-ray photoelectrons spectroscopy (XPS), Raman spectroscopy, and UV–Vis spectroscopy. The SEM images revealed two forms of flower-like nanostructures, namely lotus- and tulip-like flower ZnO nanostructures. The XPS analysis revealed the oxidation state of the Zn and O elements, as well as the presence of OH groups on the surface of the lotus-like flower ZnO nanostructure. The XRD results revealed less crystallinity of the lotus-like ZnO nanoflowers (NFs) compared with the tulip-like ZnO NFs. The XRD results revealed the presence of Zn $(OH)_2$ in the ZnO NFs. The Raman results confirmed less crystallinity of the lotus-like ZnO NFs. The estimated optical bandgap was 2.92 and 3.0 eV for the tulip- and lotus-like ZnO NFs, respectively. The tulip-like ZnO NFs showed superior photocatalytic degradation of methylene blue dye, verified via UV–Vis radiation, compared with the lotus-like ZnO NFs, which show the impact of the structure defects and OH- impurities on the photocatalytic performance of ZnO nanoflowers.

Keywords: ZnO nanoflower; structure defects; $Zn(OH)_2$; optical properties; photocatalytic

check for updates

Citation: Abdel-Fattah, E.M.; Alshehri, S.M.; Alotibi, S.; Alyami, M.; Abdelhameed, D. Hydrothermal Synthesis of ZnO Nanoflowers: Exploring the Relationship between Morphology, Defects, and Photocatalytic Activity. *Crystals* **2024**, *14*, 892. https://doi.org/10.3390/cryst14100892

Academic Editor: Alessandro Vergara

Received: 11 September 2024
Revised: 8 October 2024
Accepted: 9 October 2024
Published: 14 October 2024

Copyright: © 2024 by the authors. Licensee MDPI, Basel, Switzerland. This article is an open access article distributed under the terms and conditions of the Creative Commons Attribution (CC BY) license (https://creativecommons.org/licenses/by/4.0/).

1. Introduction

Transition metal oxide semiconductors, including both II–VI and other groups, are widely recognized for their high chemical and mechanical stability, biocompatibility, and non-toxicity [1–4]. They are attractive candidates for numerous technological applications, including biomedical devices, solar cells, gas sensors, piezoelectric devices, ceramics, drug-delivery systems, and photocatalysts [5–9]. Among these, the photocatalytic degradation of organic pollutants has garnered significant attention as a simple, eco-friendly, and highly effective method for the complete breakdown of organic dyes. ZnO nanostructures have been extensively studied for photocatalysis due to their abundance, low cost, high photosensitivity, and long-term stability [1]. ZnO nanostructures have been synthesized using various methods, including wet chemical approaches, hydrothermal techniques, sol–gel processes, microwave-assisted synthesis, biological methods, mechanical milling, and laser ablation [10–15]. Notably, the hydrothermal method has attracted attention for its energy efficiency and environmental friendliness, as it operates under closed-system conditions [10].

For photocatalyst applications, a ZnO nanoparticle (NP) has a bandgap energy of 3.1–3.3 eV that allows good absorption of UV light. Furthermore, the abundant existence of free electrons in the conduction band and the low number of holes in the valence

band [16] favor the use of ZnO nanostructures as a photocatalyst for organic dyes pollution. One strategy to improve the photocatalytic performance of ZnO nanoparticles is the rational design and controllable synthesis of ZnO with specific morphological configurations [17]. Zinc oxide (ZnO) nanostructures exhibit a wide range of morphologies, including nanorods, nanowires, nanoflowers, nanosheets, nanospheres, and hierarchical assemblies, each of which significantly influences their physicochemical properties and, consequently, their photocatalytic performance [1]. The morphology of ZnO affects key parameters such as the surface area, porosity, crystallographic orientation, defect density, and bandgap energy [18]. For instance, one-dimensional structures like nanorods and nanowires facilitate charge separation and transport due to their high aspect ratio, reducing the electron–hole recombination and enhancing the photocatalytic efficiency. Two-dimensional structures like nanosheets, on the other hand, offer a large surface area and abundant active sites, which are advantageous for pollutant adsorption and light absorption. Hierarchical structures, such as nanoflowers, combine the benefits of both 1D and 2D morphologies, providing increased surface area and efficient charge transport pathways [19]. To date, various forms of 3D ZnO have been synthesized, such as fluffy-like 3D ZnO nanoflowers [20–22], nanorods assembled into 3D microflowers [23], flower-like ZnO microspheres [24], and hollow nanorods assembled into ZnO microflowers [25]. The optimal form of a ZnO microflower for a given application depends on the specific requirements of that application.

Despite significant advances in the synthesis and application of ZnO nanostructures, the relationship between morphology, surface chemistry, and photocatalytic performance is not yet fully understood. Factors such as the role of surface defects, the influence of different crystallographic facets, and the impact of morphology on the generation and migration of charge carriers require further investigation. Addressing these challenges is crucial for optimizing ZnO nanostructures for applications in environmental remediation and pollutant degradation. Continued research is essential for gaining a deeper understanding of the physicochemical interactions and to design ZnO nanostructures with tailored properties that maximize the photocatalytic efficiency while minimizing the drawbacks like photocorrosion and recombination losses.

In the current work, we present a simple route for synthesizing a new submicron 3D ZnO flower-like structure assembled by nanoparticles and nanoplates using a hydrothermal technique. The synthesized parameters such as the growth time, temperature, Zn precursor, and capping agent were controlled and adjusted for a perfect 3D ZnO morphology. The structure, morphology, chemical composition, and spectroscopic characteristics of the synthesis of submicron ZnO flower structures were characterized by different techniques, and their photocatalytic activity of methylene blue (MB) dye degradation under visible light was evaluated.

2. Materials and Methods

2.1. Materials and Synthesis Processes

All the chemicals used in this work were of analytical grade and were used without further purification. The hydrothermal synthesis method enables the fabrication of nanostructures from low-temperature aqueous solutions under high vapor pressure. For the synthesis of lotus-flower-like ZnO nanostructures, a 0.05 M solution of zinc nitrate ($Zn(NO_3)_2$) was prepared by dissolving the appropriate amount in 100 mL of deionized water under continuous stirring. Then, a 0.075 M solution of NaOH was added to adjust the pH to 11. The solution was transferred into a sealed Teflon-lined autoclave (Zhengzhou, China) 50 mL in size) and kept in an electric furnace at 160 °C for 8 h.

For the synthesis of tulip-flower-like ZnO nanostructures, a 0.05 M solution of zinc chloride ($ZnCl_2$) was prepared by dissolving the appropriate amount in 100 mL of deionized water. This solution was then mixed with a 0.0028 M solution of cetyltrimethylammonium bromide (CTAB) under stirring. The pH of the resulting mixture was adjusted to 10 by adding a 0.075 M solution of NaOH. The solution was transferred into a sealed Teflon-lined autoclave and kept in an electric furnace at 120 °C for 4 h. After the synthesis, the autoclave

was allowed to cool naturally to room temperature. The product was harvested by filtration, washed several times with deionized water to remove any residual ions, and then dried at 60 °C for 24 h. The final product was collected for further use.

The chemical reactions involved in the synthesis of ZnO nanostructures, which resemble lotus and tulip flowers, are as follows

$$Zn(NO_3)_2 + 2NaOH \rightleftharpoons Zn(OH)_2 + 2NaCl$$

$$ZnCl_2 + 2NaOH \rightleftharpoons Zn(OH)_2 + 2NaCl$$

$$Zn(OH)_2 \rightarrow ZnO + H_2O$$

2.2. Characterization and Photocatalytic Measurements

The ZnO flower-like nanostructures were characterized using various techniques: scanning electron microscopy (SEM) (Thermo Fisher Quanta FEG250 SEM, Hillsboro, OR, USA) was used for morphology; an X-ray diffractometer (XRD) (Rigaku International Corp., Tokyo, Japan) with Cu Ka radiation of λ = 1.543 A in the 2 θ range from 10° to 80° was used for the microstructure; micro Raman (SENTERRA II-BRUKER, Carteret, NJ, USA) spectrometry, at a wavelength of 532 nm, a spectral resolution of 5 cm^{-1}, with a specified laser spot size of 2 μm, and a power of 6.25 mw, was used for the vibrational characteristics; the chemical composition of syntheses samples was examined by X-ray photoelectron spectroscopy (XPS), Thermo K Alpha spectrometer (XPS Thermo Scientific, Waltham, MA, USA), with a spot size of 400 microns and charge correction employing Al K alpha X-rays; a UV-5200 spectrophotometer (Shenzhen, China) was used to determine the optical properties of the ZnO flower-like nanostructures; the photocatalytic activity of ZnO was evaluated by the degradation of methylene blue dye; the fluorescence spectra were recorded using a laser wavelength of 350 nm using a fluorescence spectrophotometer (LS-55, Perkin Elmer, Waltham, MA, USA); the texture properties of the ZnO NFs were recorded using Quantachrome Autosorb iQ3 (Anton Paar, Graz, Austria).

All photocatalytic experiments were performed in a batch photoreactor using a UV–Vis light source (248–579 nm) with an 80 W high-pressure mercury lamp (HPML) from LD DIDACTIC (Huerth, Germany). The lamp was positioned perpendicularly to the reaction beaker. In each experiment, 0.2 g/L of ZnO nanoflowers (NFs) were suspended in 60 mL of a methyl blue dye solution (10 mg/L). The solution was stirred in the dark for 30 min to reach adsorption–desorption equilibrium. Afterwards, the suspension was directly exposed to the mercury lamp while being continuously stirred. After a specific interval, 5 mL of the reaction suspension was withdrawn using a 3 μm needle. Measurements were taken every 20 min, starting with the dark sample (0 min). The absorbance of the MB solutions was measured using a UV–Visible absorption spectrophotometer (UV5200).

3. Results

3.1. Morphology and Structure Properties

Figure 1 shows an SEM image of the as-synthesized flower-like ZnO nanostructures. The image was analyzed using ImageJ software (version 1.54j) to estimate the size of the nanoflowers (NFs), as well as the sizes of the nanopetals and nanoparticles, as shown in the inset of Figure 1. The zinc precursor and reaction temperature play a crucial role in determining the morphology of the synthesized ZnO samples. Figure 1a reveals highly uniform lotus-like ZnO nanostructures. Each nanoflower has an average size of approximately 1–1.5 μm, resembling a fully bloomed flower composed of leaf-like petals (350–400 nm in length) radiating from a central hexagonal cluster (Figure 1b). These nanopetals are made up of fine nanoparticles, approximately 20–40 nm in size, which aggregate electrostatically to form a petal-like arrangement (inset Figure 1b). Figure 1c illustrates a different morphology, resembling tulip-like ZnO nanostructures, characterized by the irregularly shaped nanosheets agglomerated in a flower-like arrangement. The average size of the tulip-like ZnO nanoflowers is 1.5–2 μm, as shown in the inset of Figure 1c. The nanosheets

are approximately 20 nm thick, with lengths ranging from 200 to 400 nm, as shown in the inset of Figure 1d. The ZnO nanosheets possess a high surface area and active edge sites that facilitate the mobility of charge carriers [26], which is an important criterion for sunlight-driven photocatalyst materials.

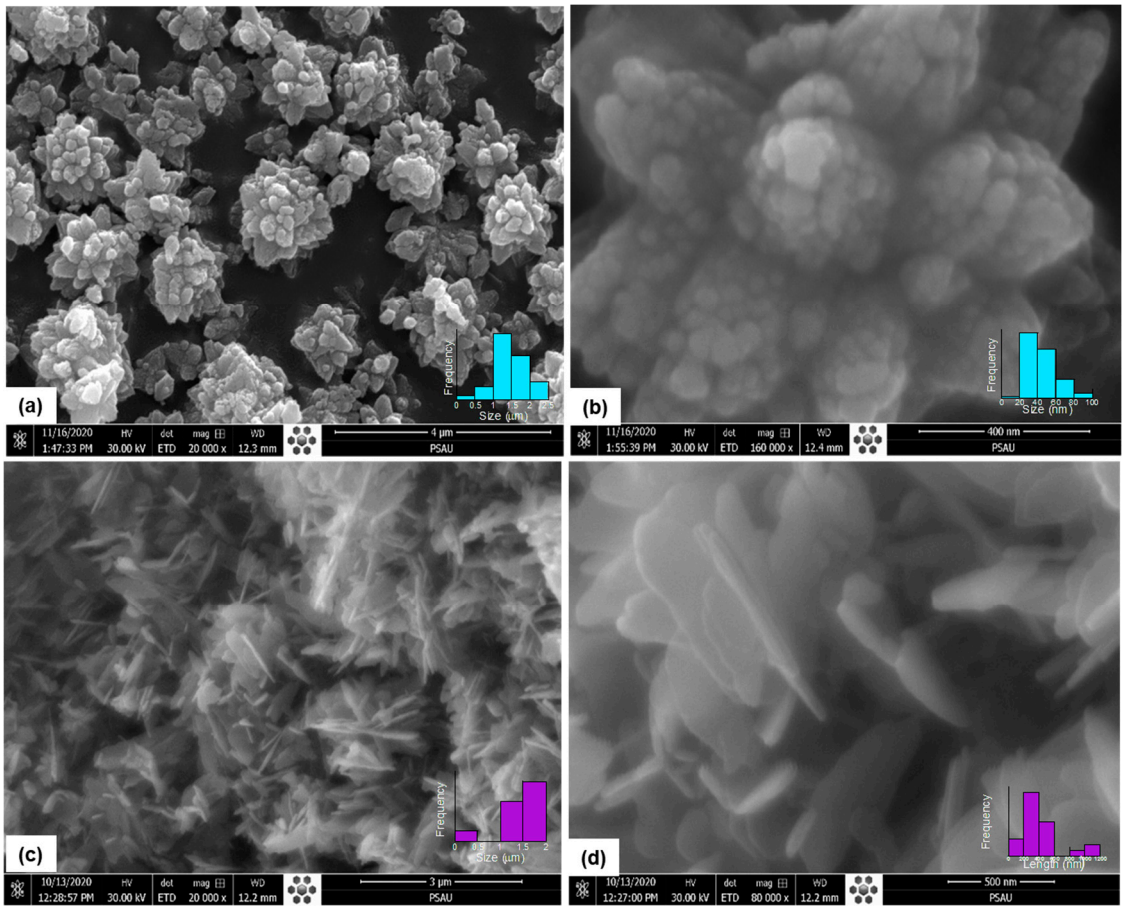

Figure 1. FE-SEM images of the synthesized ZnO (**a**,**b**) lotus- and (**c**,**d**) tulip-like ZnO nanoflowers at different magnifications.

Figure 2a presents the XRD patterns of the lotus- and tulip-flower-like ZnO nanostructures. The XRD pattern of the tulip nanoflower reveals a well-defined crystalline structure, with several sharp peaks of varying intensities centered at 2 θ~31.7°, 34.4°, 36.2°, 46.87°, 56.0°, 62.2°, and 67.3°. These correspond to the hexagonal wurtzite ZnO structure with the space group P63mc (card number 96-900-8878). These peaks are attributed to the (100), (002), (101), (102), (110), (103), and (112) planes, respectively. In contrast, the XRD peaks of the lotus-flower-like ZnO nanostructure display lower intensities and are shifted towards smaller diffraction angles compared to those of the tulip f-like ZnO, suggesting an increase in lattice parameters and/or structural defects. Additionally, the XRD peaks of the lotus-flower-like ZnO at 2 θ~30.9° and 33.6° correspond to zinc hydroxide, $Zn(OH)_2$ (card number 96-451-7838), indicating that the lotus-flower-like ZnO consists of both zincite and zinc hydroxide. The lotus-flower-like ZnO nanostructure exhibits a crystalline structure with trigonal symmetry and hexagonal axes (card number 96-152-8231), which explains the shift towards lower 2θ values.

Both samples exhibit a preferential growth orientation along the (101) plane. However, the moderate intensity of (002) peak suggests that the ZnO nanopetals/nanosheets also grow along the c-axis. The crystalline size, D, was determined using the Scherer formula, $D = \frac{0.9 \cdot \lambda}{\beta \cdot \cos\theta}$, where λ is the X-ray wavelength (λ = 1.543 Å), and β is the full width at half maximum (FWHM) of the (002) peak at angle θ. The lattice parameter a and c were calcu-

lated using the relations $a = \frac{\lambda}{1.73 \cdot \sin\theta_{100}}$ and $c = \frac{\lambda}{\sin\theta_{200}}$, respectively [15]. The calculated crystalline size and lattice parameters are summarized in Table 1.

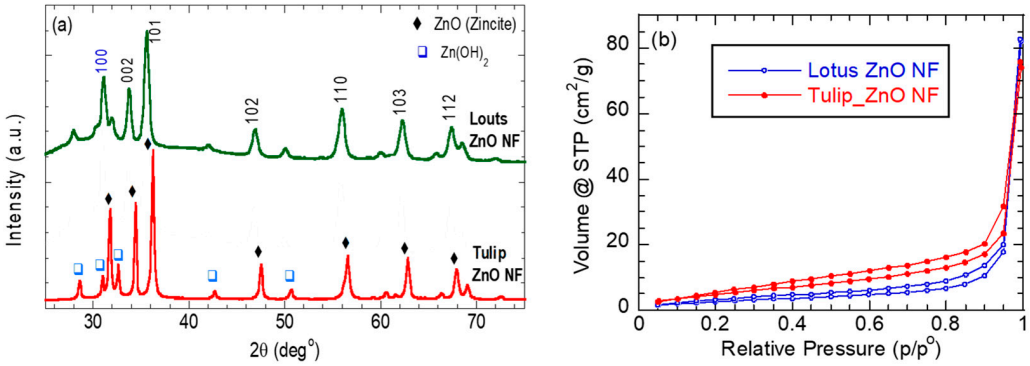

Figure 2. (**a**) XRD patterns and (**b**) of the synthesized tulip- and lotus-flower-like ZnO nanostructures.

Table 1. XRD pattern analysis of lotus- and tulip-flower-like nanostructures.

Sample	Crystal Size (nm)	*a* (Å)	*c* (Å)
Lotus-flower-like Nanostructures	15.92	3.322	5.3190
Tulip-flower-like Nanostructures	28.72	3.2495	5.2069

The calculated lattice parameter c is slightly higher than that of bulk ZnO (*c* = 5.205 Å). This indicates that the ZnO flower-like nanostructures are under tensile strain, particularly along the c-axis, with the lotus-flower-like ZnO nanostructure showing pronounced strain in this direction.

Figure 2b displays the N_2 adsorption–desorption isotherms of the ZnO nanoflowers (NFs) examined at room temperature. The ZnO NF samples exhibit a typical type IV isotherm hysteresis loop, according to the IUPAC classification. The isotherms span a wide p/p_0 range (0.2–0.90), indicating a mesoporous structure. The isotherm of the tulip ZnO NFs demonstrates a higher N_2 uptake compared to that of the lotus ZnO NFs, suggesting a greater surface area and porosity. Specifically, the BET surface area of the tulip ZnO NFs is 13.43 m^2/g, while that of the lotus ZnO NFs is 8.0 m^2/g.

3.2. Chemical Composition and Vibrational Analysis

Figure 3a shows the survey XP spectra of as-synthesized lotus- and tulip-shaped ZnO nanoflowers. The prominent Zn $2p_3/_2$, Zn $2p_1/_2$, and O 1s peaks confirm that both ZnO nanoflowers (NFs) are primarily composed of zinc and oxygen. The relative intensities of the Zn 2p and O 1s peaks correspond to the concentrations of Zn and O, respectively. Additional XPS spectral lines, such as Zn 3d, Zn 3s, and Zn LMM (Auger) peaks, were also detected [27]. The absence of any other elemental peaks in the XP spectra indicates the purity of the ZnO NFs, in agreement with the XRD results.

To identify the oxidation state of the ZnO nanoflowers, high-resolution spectra of O 1s and Zn 2p were obtained, as shown in Figure 3b,c. The O 1s spectrum of both samples is asymmetric, with a shoulder at higher binding energy (B.E.). For the lotus-like ZnO nanostructure, the O 1s spectrum decomposes into three sub-peaks: 529.8 eV, assigned to hexagonal Zn^{2+} ions bonded to O^{2-} in the wurtzite ZnO crystal structure (Zn–O); 531.3 eV, attributed to defects or the presence of oxygen vacancies [28]; and 532.3 eV, associated with adsorbed OH^- species on the surface [29]. A similar deconvolution is observed for the O 1s spectrum of the tulip-like ZnO nanostructure, yet without the peak at 532.3 eV, which is assigned to Zn–OH. The XRD results (Figure 2) further confirm the presence of OH^- species in the lotus-like ZnO nanoflowers. The high-resolution Zn 2p spectrum of (Figure 3c) reveals strong spin–orbit coupling, with Zn $2p_3/_2$ and Zn $2p_1/_2$ peaks, corresponding to Zn atoms at the regular lattice sites in ZnO [30]. For the tulip-like ZnO

nanostructure, the Zn $2p_3/_2$ and Zn $2p_1/_2$ peaks are located at 1020.9 eV and 1044.0 eV, respectively. In contrast, for the lotus-like structure, these peaks shift slightly to lower B.E. values of 1020.8 eV and 1043.9 eV, respectively. The binding energy, separation, and ΔE (Zn 2p), are 23.1 eV, which is characteristic of ZnO [31]. The observed peak shift in the Zn 2p spectrum of the lotus-flower-like structure compared to that of the tulip-flower-like structure could be related to the variations in morphology, as observed in the SEM images. A similar observation was reported in [32].

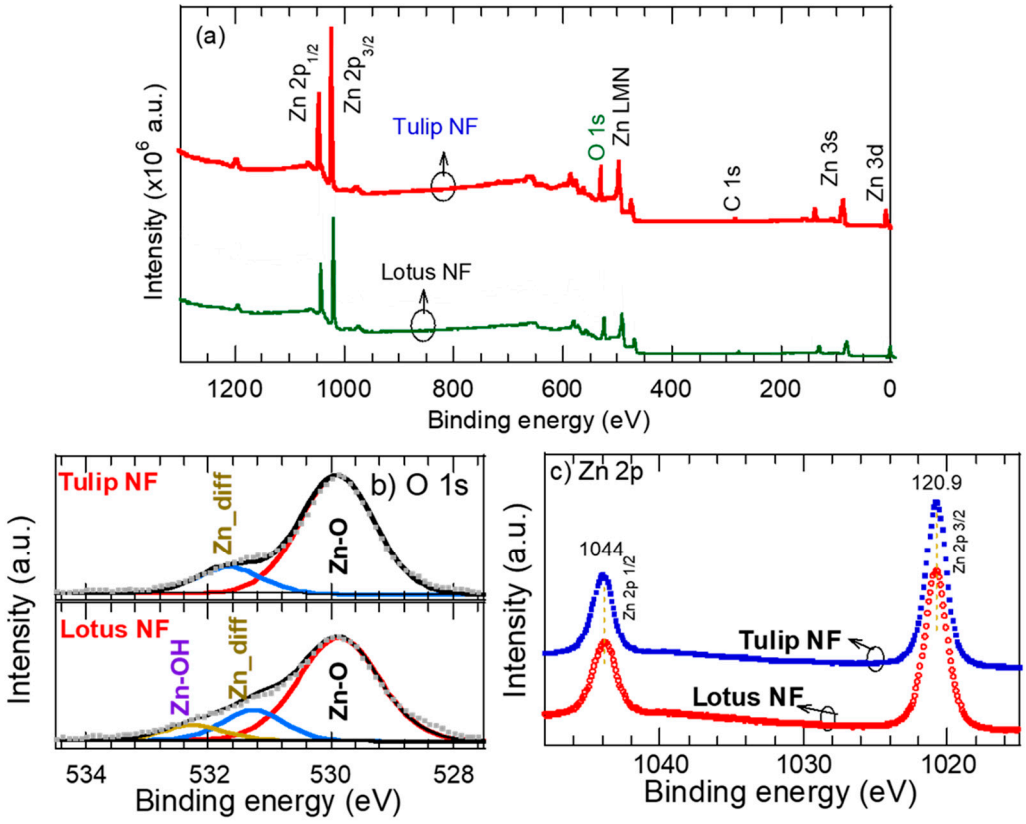

Figure 3. (**a**) Survey spectra and high-resolution spectra for (**b**) oxygen O 1s and (**c**) Zn 2p of lotus- and tulip-like ZnO nanoflowers.

The vibrational properties of the synthesized ZnO nanoflower-like structures were investigated using a green laser with a wavelength of λ = 532 nm at room temperature, with the results shown in Figure 4. Raman modes characteristic of ZnO are present in both samples at 98.5, 334, 390, 438.5, 538, and 577.5 cm^{-1}. These peaks correspond to Raman modes of ZnO in the hexagonal wurtzite structure: E_2 (Low), E_2 (High)–E_2 (Low), A_1 (TO), E_2 (High), A_1 (LO), and E_1 (LO) modes, respectively [15]. The slight shift in the Raman mode positions of the lotus flower sample, compared with the tulip-flower-like sample, is attributed to tensile stress on the lattice structure, as inferred from the XRD analysis. Additionally, the small humps observed in the Raman spectra of the lotus flower sample at ~260, 380, and 700 cm^{-1} are attributed to $Zn(OH)_2$ modes [33].

The E_2 (low) peak is ascribed to vibrations of the zinc sublattice in ZnO [34], while the most intense and asymmetric E_2 (high) mode is linked oxygen vibrations and serves as an indicator of the crystallinity of the wurtzite ZnO nanostructure [34]. The intensities of the E_2 (high) mode in both samples correspond well with the XRD results, suggesting that the lotus flowers-like ZnO nanostructure (Figure 4b) exhibits lower crystallinity than the tulip-flower-like ZnO sample. Additionally, the small peaks labeled E_2 (high)–E_2 (low), A_1 (TO), and A_1 (LO) represent vibration modes resulting from a multiple-phonon scattering process [35]. The E_1 (LO) mode indicates the presence of oxygen-deficient intrinsic defects [36]. These findings align well with the XRD measurements, as the strong E_2 (high) mode and the

weak E_1 (LO) peak demonstrate that the tulip-flower-like ZnO nanostructures has a higher crystallinity compared to the lotus-flowers-like ZnO nanostructure.

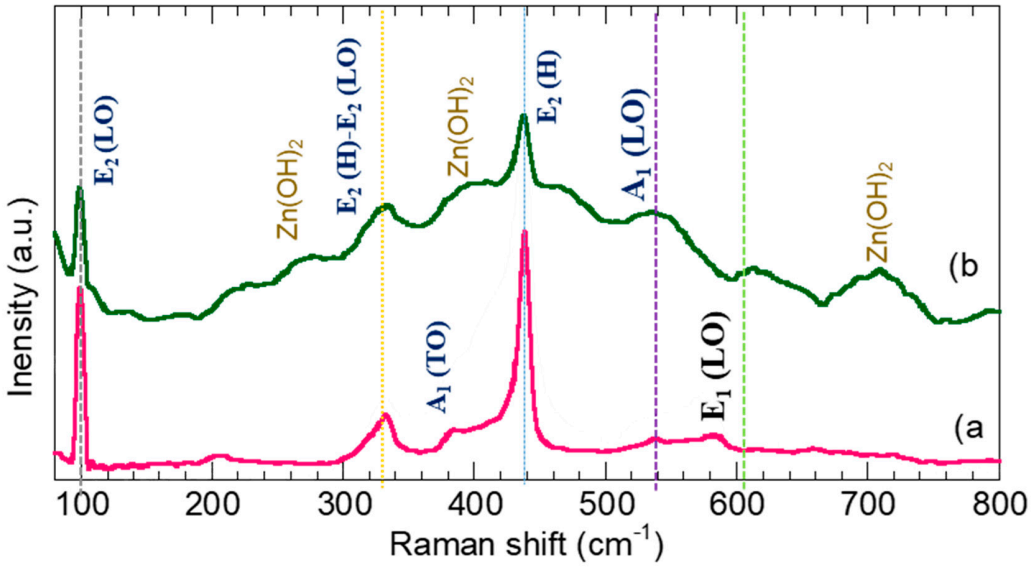

Figure 4. Raman spectra of the synthesized (**a**) tulip- and (**b**) lotus-flower-like ZnO nanostructures.

3.3. Optical and Photoluminescent Properties

Figure 5 shows the absorption spectra of the as-synthesized flower-like ZnO nanostructures. Both types of flower-like ZnO nanostructures demonstrate strong absorption in the UV region (<<400 nm). The UV absorption peaks are observed at 373 nm and 374 nm for the tulip and lotus-flower-like ZnO nanostructures, respectively. These values are lower than the 380 nm absorption peak of bulk ZnO, suggesting the presence of a quantum size effect [37].

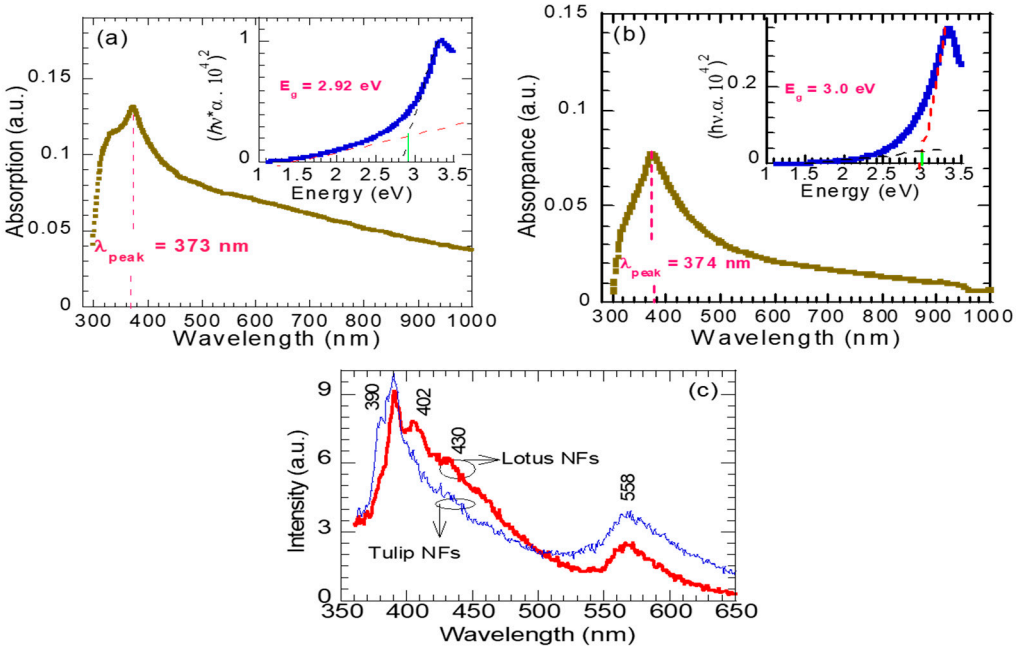

Figure 5. UV–Visible optical absorption and plots of $(h\nu.\alpha)^2$ versus hν of the synthesized (**a**) tulip- and (**b**) lotus-flower-like ZnO nanostructures. (**c**) PL spectra of ZnO NFs.

Furthermore, the enhanced absorption in the UV range is attributed to the intrinsic bandgap absorption of ZnO [38]. Additionally, the tulip-like ZnO nanostructures demon-

strate higher absorption in the near visible range compared to their lotus-like counterparts. This broad absorption spectrum is likely due to the complex 3D nanoflower shape, which consists of assembled nanoparticles (ranging from 23 nm to 73 nm) and nanosheets (~20 nm thick and 100 nm long) that form agglomerated flower-like structures. As a result, the diverse sizes and shapes of these nanostructures contribute to their wide absorption spectrum.

The optical bandgap energy (E_g) of the synthesized ZnO nanoflowers was estimated using Tauc's law [15].

$$h\nu \cdot \alpha = A \cdot (h\nu - E_g)^n \quad (1)$$

where α is the absorption coefficient, $h\nu$ is the photon energy, A is a constant, and n = 2 is the direct bandgap. The value of E_g is obtained by extrapolating the linear extension of $(h\nu.\alpha)^2$ versus $h\nu$ to $h\nu = 0$. The α was taken from the absorption spectrum. From the inset of Figure 5, the E_g values were found to be 2.92 and 3.0 eV for the tulip- and lotus-like ZnO nanostructures, respectively. The estimated E_g values indicate that the required photon wavelength for photocatalytic processes is ~>>413~424 nm, which aligns with the lower edge of the visible region. The E_g values for the tulip- and lotus-flower-like ZnO nanostructures are lower than that of bulk ZnO (E_g = 3.37 eV) [39]. The reduction in E_g values for the ZnO nanoflowers compared to bulk ZnO can likely be attributed to the presence of structure defects and/or oxygen vacancies, as observed in the XPS and Raman results [40]. This suggests the potential for solar driven photocatalysis of the 3D-ZnO nanoflowers, particularly the tulip-like ZnO nanostructures.

Figure 5c presents the photoluminescence (PL) spectra of ZnO NFs at room temperature, using an excitation wavelength of 350 nm. Irrespective of the type of ZnO NFs, the PL spectra display two prominent emission bands. The first band, located in the UV region at 390 nm, arises from the recombination of exciton [41]. The second band, which is broad and found in the green visible region at 558 nm, is attributed to the presence of point defects, such as interstitial oxygen and oxygen vacancies [42]. Further, the lotus ZnO NFs exhibit additional peaks in the violet region at 402 and 430 nm, which originate from zinc interstitial [43]. The tulip ZnO NFs show a stronger green emission compared to the lotus ZnO NFs, suggesting a higher concentration of oxygen vacancies in the tulip ZnO NFs.

3.4. Photocatalytic Activity

Figure 6a presents the photolysis of MB, while Figure 6b,c show the photocatalytic degradation of MB dyes under UV–Vis light irradiation using ZnO nanoflower solutions. As observed, MB exhibits characteristic absorption bands at 667 nm and 608 nm, corresponding to the MB monomer and dimer, respectively. Upon exposure to UV–Vis light, a significant reduction in the intensity of these absorption bands is seen, indicating effective degradation of MB. Since the intensity of the absorbance peak is proportional to the concentration of MB molecules, the decline in band intensity suggests the degradation of MB molecules. The absorption bands of MB completely disappear after 80 min of irradiation with the tulip-like ZnO nanoflower (NF) catalyst. In contrast, both photolysis and lotus-like ZnO NF catalyst shows a much slower reduction in MB intensity, which remains clearly visible even after 100 min of irradiation. The UV–Vis absorption spectra reveals that the tulip-like ZnO NF has a broader absorption range compared to the lotus-like ZnO NF, which likely contributes to its superior photocatalytic performance in MB degradation. Furthermore, the sharp edges of the nanosheets in the tulip-like ZnO NF enhance charge carrier mobility [28], further boosting its catalytic efficiency.

Moreover, the MB monomer peak at 667 cm^{-1} shifts towards lower wavelengths (a blue shift) as exposure time increases, particularly with the tulip-like ZnO NF, as shown in Figure 6a. This blue shift in the MB peak indicates the breakdown of the conjugated system, resulting in the formation of safer byproducts [44]. Figure 6d shows the normalized absorbance $\left(\frac{A_t}{A_o}\right)$ of ZnO NFs as a function of the exposure time, where A_o is the initial MB absorption and A_t is the MB absorption after exposure with light at a specified time. The tulip-like ZnO NFs clearly demonstrate a higher photodegradation rate over the entire

reaction time. The degradation efficiency calculated as % Degradation $= \frac{A_o - A_t}{A_o} \times 100$ was found to be 7.8% after 100 min of UV–Vis irradiation without ZnO NFs. In the presence of lotus-like and tulip-like ZnO NFs, the degradation efficiency increased to 40% and 90%, respectively. The degradation efficiency reported for the tulip-like ZnO NF is higher than previously reported values for ZnO-nanoflowers in MB degradation [23,26].

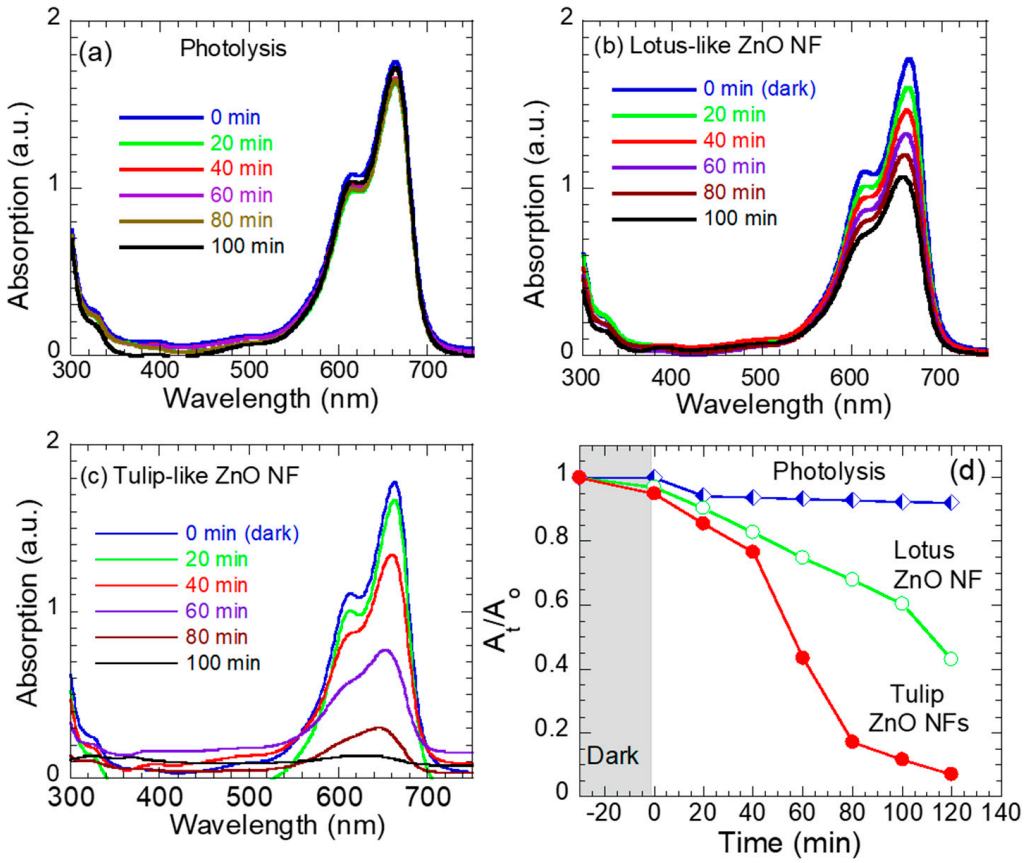

Figure 6. Absorption spectra of MB dye mixture with (**a**) photolysis of MB, (**b**) tulip-like ZnO NFs, (**c**) lotus-like ZnO NFs as function of exposure time, and (**d**) normalized absorbance (A_t/A_o) of ZnO nanoflowers in MB solution as a function of exposure time.

The mechanism of degradation MB using ZnO NF-like structures under UV–Vis radiation is depicted in Figure 7 and summarized by Equations (2)–(6). The empirical formulas $E_{VB} = \chi - E_c + 0.5\, E_g$ and $E_{CB} = E_{VB} - E_g$, are employed to determine the positions of the valence band (VB) and conduction band (CB) based on the optical bandgap energy E_g values [45]. Here, χ = 5.89 eV represents the electronegativity of ZnO, and E_c = 4.5 eV is the energy of free electrons on the hydrogen scale. The estimated positions of the CB and VB for tulip-like and lotus-like ZnO NFs are depicted in the energy diagram in Figure 7a. Regardless of the NF type, holes in the VB with a potential greater than 2.32 can generate hydroxyl radicals OH. Similarly, the CB position is more negative than the O_2/O_2^- redox potential, i.e., allowing electrons to readily interact with O_2.

$$ZnO + h\nu \longrightarrow ZnO\left({e_{CB}}^- + {h_{VB}}^+\right) \quad (2)$$

$${e_{CB}}^- + O_2 \longrightarrow O_2^- \quad (3)$$

$${h_{VB}}^+ + OH^- \longrightarrow OH \quad (4)$$

$$O_2^- + 2H^+ \longrightarrow 2 \cdot OH \quad (5)$$

$$OH + MB \longrightarrow decomposed\ material \quad (6)$$

Briefly, when the ZnO nanoflowers (NFs) are exposed to light with photons energy $h\nu \geq E_g$, the adsorbed photons generate electron (e^-)–hole (h^+) pairs. The electrons in the conduction band (CB) and the holes in the valence band (VB) migrate to the surface of ZnO NFs. The electrons reduce molecular oxygen O_2 on the ZnO NFs surfaces, forming super-oxide anions (O_2^-). Simultaneously, the holes oxidize water (H_2O) or hydroxide ions OH^- adsorbed on ZnO NFs, producing hydroxyl radicals OH [46]. The O_2^- can further react with protons (H^+), generating additional hydroxyl radicals These hydroxyl radicals then interact with the adsorbed methylene blue (MB) molecules, causing decolorization of MB and possible degrading it into harmless components. In this experiment, the tulip-like ZnO NFs morphology, along with their optical and structure properties, contribute to their superior photocatalytic performance in the possible degradation of MB compared to the lotus-like ZnO NFs.

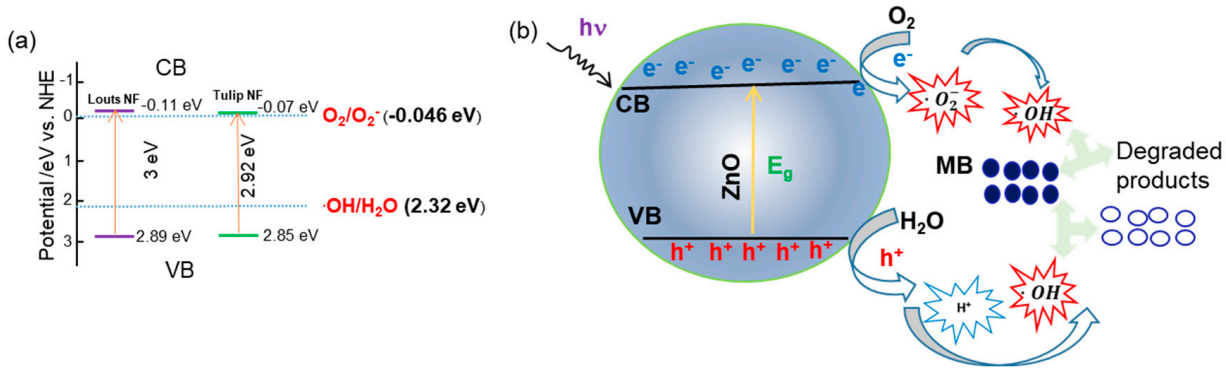

Figure 7. (**a**) Schematic band diagrams of ZnO NFs display the charge transportation processes leading to photocatalytic degradation of MB dyes; (**b**) MB degradation mechanism in the presence of ZnO NFs.

3.5. Photo-Degradation Kinetic

The mechanisms governing the degradation kinetics of methylene blue (MB) dye in the presence of ZnO nanoflowers (NFs) catalysts were analyzed using zero-order, pseudo-first-order, and pseudo-second-order kinetic models. The integrated forms of these kinetic models are as follows [47]:

Zero-order, $A_t = A_o - k_o t$

1st-order, $A_t = A_o e^{-k_1 t}$

2nd-order, $\frac{1}{A_t} = \frac{1}{A_o} + k_2$

In these equations, A_o and A_t represent the absorbance of MB at the initial time and at time t, respectively. k_o, k_1, and k_2 are the rate constants for zero-order, first-order, and second-order reactions, respectively. The absorbance values of MB at various time intervals (Figure 6b,c) were used to calculate these constants.

To identify the most suitable kinetic model, plots of A_t, Ln (A_o/A_t), and $1/A_t$ versus time were graphed (see Figure 8a–c). The correlation coefficient (R^2) of the linear fit for each model was evaluated, and the slope of the linear fit provides the rate constants. The kinetic parameters for all three models are summarized in Table 2.

As shown in Table 2 and illustrated in Figure 7, both the zero-order and pseudo-first-order models exhibit the highest R^2 values compared to the pseudo-second-order model. Therefore, we conclude that these two models are the most suitable for representing the photocatalytic degradation of methylene blue (MB).

Furthermore, the estimated rate constants, k_o, k_1, and k_2, for the degradation process using ZnO tulip NFs demonstrate superior reactivity as photocatalyst compared to ZnO-lotus-like NFs.

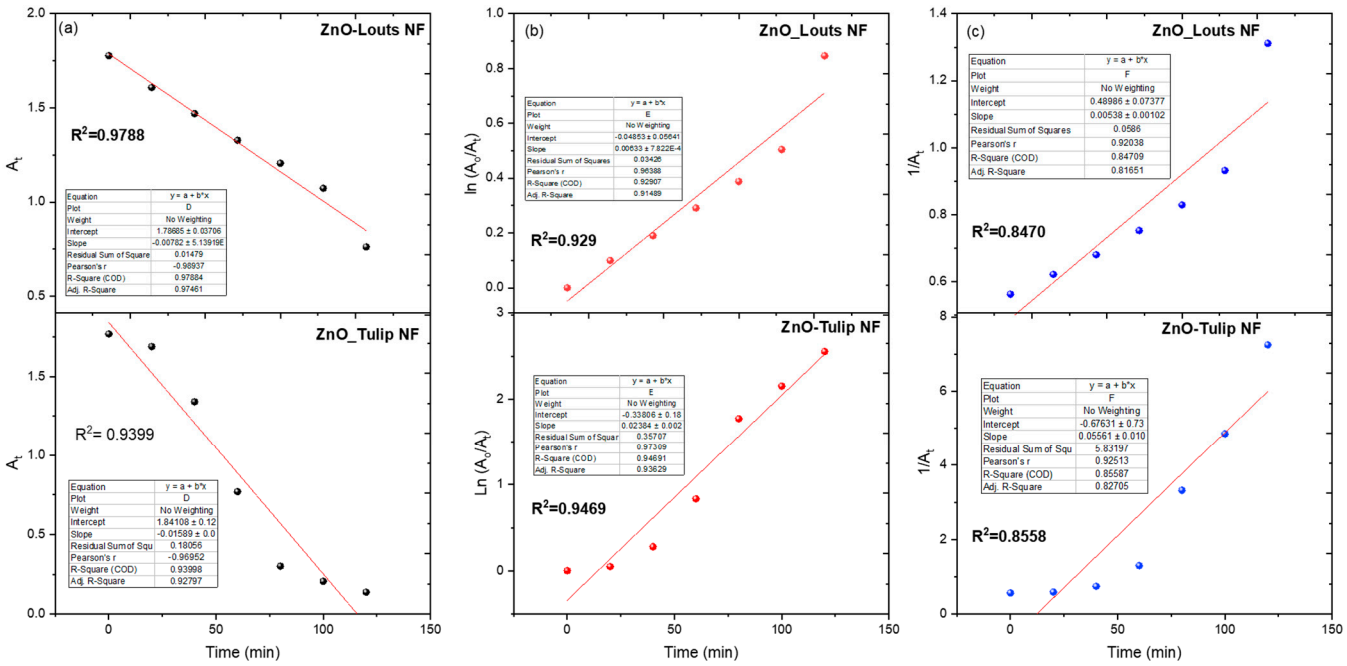

Figure 8. The plots of (**a**) A_t, (**b**) ln (A_o/A_t), and (**c**) ($1/A_t$) versus time along with their linear fits for MB dye in presence of ZnO NFs as photocatalysts.

Table 2. Kinetic rate constants and correlation coefficients of MB dye degradation in the presence of ZnO NFs.

Scheme	Kinetic Model Parameters		
	Zeroth Order	**Pseudo-First Order**	**Pseudo-Second Order**
ZnO-lotus NFs	K_o = 0.00782	K_1 = 0.00633	K_2 = 0.0538
	R^2 = 0.9788	R^2 = 0.929	R^2 = 0.8470
ZnO-tulip NFs	K_o = 0.01589	K_1 = 0.0238	K_2 = 0.05561
	R^2 = 0.9399	R^2 = 0.9469	R^2 = 0.8558

4. Conclusions

In summary, two forms of ZnO flower-like nanostructures were synthesized through a hydrothermal method under different conditions: lotus- and tulip-like ZnO nanostructures. The lotus-like ZnO (NF) resembles a fully bloomed flower, with nanopetals radiating from a central core. In contrast, the tulip-like ZnO (NF) consists of irregular nanosheets forming a flower-like agglomeration. XRD analysis revealed that the tulip-like ZnO (NF) has a wurtzite hexagonal structure, while the lotus-like ZnO (NF) exhibits a trigonal crystalline structure with hexagonal axes. XPS data confirmed the oxidation state of Zn^{2+} and suggested the possible presence of oxygen vacancies. Both ZnO (NFs) samples appear to be a mixture of oxide and hydroxide ZnO form, as indicated by the XRD results. The tulip-like ZnO showed a broader absorption range compared to the lotus-like ZnO, which correlates on their enhanced performance in MB degradation under UV–Vis light.

Author Contributions: Conceptualization, E.M.A.-F.; methodology, E.M.A.-F., S.M.A., S.A. and M.A.; validation, E.M.A.-F., S.M.A., S.A. and M.A.; formal analysis, E.M.A.-F., S.A. and M.A.; investigation, E.M.A.-F., S.A., M.A. and D.A.; writing—original draft preparation, E.M.A.-F.; writing—review and editing, E.M.A.-F., S.A., M.A. and D.A. All authors have read and agreed to the published version of the manuscript.

Funding: This study is supported via funding from Prince sattam bin Abdulaziz University project number (PSAU/2024/R/1446).

Data Availability Statement: The authors confirm that the data supporting the findings of this study are available within the article.

Conflicts of Interest: The authors declare no conflicts of interest.

References

1. Radzimska, A.K.; Jesionowski, T. Zinc Oxide—From Synthesis to Application: A Review. *Materials* **2014**, *7*, 2833–2881. [CrossRef]
2. Farooq, U.; Ruby Phul, R.; Alshehri, S.M.; Ahmed, J.; Ahmad, T. Electrocatalytic and Enhanced Photocatalytic Applications of Sodium Niobate Nanoparticles Developed by Citrate Precursor Route. *Sci. Rep.* **2019**, *9*, 4488. [CrossRef]
3. Naaz, F.; Shamsi, A.; Jain, S.K.; Kalam, A.; Ahmad, T. Tin oxide nanocatalyst assisted transformation of p-Nitrophenol to p-Aminophenol. *Mater. Today Proc.* **2021**, *36*, 708–716. [CrossRef]
4. Farooq, U.; Chaudhary, P.; Ingole, P.P.; Kalam, A.; Ahmad, T. Development of Cuboidal $KNbO_3$@α-Fe_2O_3 Hybrid Nanostructures for Improved Photocatalytic and Photoelectrocatalytic Applications. *ACS Omega* **2020**, *5*, 20491–20505. [CrossRef]
5. Gupta, J.; Hassan, P.A.; Barick, K.C. Multifunctional ZnO nanostructures: A next generation nanomedicine for cancer therapy, targeted drug delivery, bioimaging, and tissue regeneration. *Nanotechnology* **2023**, *34*, 282003. [CrossRef]
6. Wibowo, A.; Marsudia, M.A.; Amal, M.I.; Ananda, M.B.; Stephanie, R.; Ardy, H.; Diguna, L.J. ZnO nanostructured materials for emerging solar cell applications. *RSC Adv.* **2020**, *10*, 42838–42859. [CrossRef]
7. Bhati, V.S.; Hojamberdiev, M.; Kumar, M. Enhanced sensing performance of ZnO nanostructures-based gas sensors: A review. *Energy Rep.* **2020**, *6*, 46–62. [CrossRef]
8. Pandey, R.K.; Dutta, J.; Brahma, S.; Rao, B.; Liu, C.-P. Review on ZnO-based piezotronics and piezoelectric nanogenerators: Aspects of piezo potential and screening effect. *J. Phys. Mater.* **2021**, *4*, 044011. [CrossRef]
9. Sheikh, M.; Pazirofteh, M.; Dehghani, M.; Asghari, M.; Rezakazemi, M.; Valderrama, C.; Cortina, J.-L. Application of ZnO nanostructures in ceramic and polymeric membranes for water and wastewater technologies: A review. *Chem. Eng. J.* **2020**, *391*, 123475. [CrossRef]
10. Kumaresan, N.; Ramamurthi, K.; Ramesh, B.R.; Sethuraman, K.; Moorthy, B.S. Hydrothermally grown ZnO nanoparticles for effective photocatalytic activity. *Appl. Surf. Sci.* **2017**, *418*, 138–146. [CrossRef]
11. Debanath, M.K.; Karmakar, S. Study of blueshift of optical band gap in zinc oxide (ZnO) nano particles prepared by low-temperature wet chemical method. *Mater. Lett.* **2013**, *111*, 116–119. [CrossRef]
12. Darr, J.A.; Zhang, J.; Makwana, N.; Weng, X. Continuous Hydrothermal Synthesis of Inorganic Nanoparticles: Applications and Future Directions. *Chem. Rev.* **2017**, *117*, 11125–11238. [CrossRef]
13. Raha, S.; Ahmaruzzaman, M.d. ZnO nanostructured materials and their potential applications: Progress, challenges, and perspectives. *Nanoscale Adv.* **2022**, *4*, 1868–1925. [CrossRef]
14. Shahzad, S.; Javed, S.; Usman, M. A Review on Synthesis and Optoelectronic Applications of Nanostructured ZnO. *Front. Mater.* **2021**, *8*, 613825. [CrossRef]
15. Abdel-Fattah, E.; Elsayed, I.A.; Fahmy, T. Substrate temperature and laser fluence effects on properties of ZnO thin films deposited by pulsed laser deposition. *J. Mater. Sci. Mater. Electron.* **2018**, *29*, 19942. [CrossRef]
16. Ma, S.; Yunyun, H.; Hong, R.; Lu, X.; Li, J.; Zheng, Y. Enhancing Photocatalytic Activity of ZnO Nanoparticles in a Circulating Fluidized Bed with Plasma Jets. *Catalysts* **2021**, *11*, 77. [CrossRef]
17. Yang, Z.; Ye, Z.; Xu, Z.B.; Zhao, B. Effect of the Morphology on the Optical Properties of ZnO Nanostructured. *Physica E Low Dimens. Syst. Nanostruct.* **2009**, *42*, 116–119. [CrossRef]
18. Kumar, P.; Singh, R.K. Influence of Morphology on the Photocatalytic Performance of ZnO Nanostructures. *Mater. Today Chem.* **2021**, *20*, 100463.
19. Xu, Y.J.; Zhuang, Y.; Wang, W.; Xiong, W. Recent advances in hierarchical micro/nanostructured ZnO and Ag/ZnO photocatalysts. *Catal. Sci. Technol.* **2017**, *7*, 4126–4139.
20. Vinod, R.; Sajan, P.; Achary, S.R.; Tomas, C.M.; Munoz-Sanjos, V.; Bushiri, M.J. Enhanced UV emission from ZnO nanoflowers synthesized by the hydrothermal process. *J. Phys. D Appl. Phys.* **2012**, *45*, 425103. [CrossRef]
21. Xu, X.L.; Chen, Y.; Ma, S.Y.; Yan, S.H.; Mao, Y.Z.; Wang, T.; Bian, H.Q. CTAB-assisted synthesis of unique 3D ZnO and the acetone sensing performances. *Mater. Lett.* **2015**, *151*, 5–8. [CrossRef]
22. Qu, Y.; Huang, R.; Qi, W.; Shi, M.; Su, R.; He, Z. Controllable synthesis of ZnO nanoflowers with structure-dependent photocatalytic activity. *Catal. Today* **2020**, *355*, 397–407. [CrossRef]
23. Zou, X.; Ke, J.; Hao, J.; Yan, X.; Tian, Y. A new method for synthesis of ZnO flower-like nanostructures and their photocatalytic performance. *Phys. Rev. B Condens.* **2022**, *624*, 413395. [CrossRef]
24. Wu, H.; Xie, Q.; An, L.; Jin, P.; Peng, D.-L.; Huang, C.; Wan, H. Facile preparation of porous flower-like ZnO microspheres with excellent photocatalytic performance. *Mater. Lett.* **2015**, *139*, 393–396. [CrossRef]
25. Duo, S.; Zhong, R.; Liu, Z.; Wang, J.; Liu, T.; Huang, C.; Wu, H. One-step hydrothermal synthesis of ZnO microflowers and their composition-/hollow nanorod-dependent wettability and photocatalytic property. *J. Phys. Chem. Solids* **2018**, *120*, 20–33. [CrossRef]
26. Cunha, D.M.; Souza, F.L. Facile synthetic route for producing one-dimensional zinc oxide nanoflowers and characterization of their optical properties. *J. Alloys Compd.* **2013**, *577*, 158–164. [CrossRef]

27. Abdel-Fattah, E.; Alotibi, S. Synergistic Effect of Nonthermal Plasma and ZnO Nanoparticles on Organic Dye Degradation. *Appl. Sci.* **2023**, *13*, 10045. [CrossRef]
28. Wang, Z.G.; Zu, X.T.; Zhub, S.; Wang, L.M. Green luminescence originates from surface defects in ZnO nanoparticles. *Physica E Low Dimens. Syst. Nanostru.* **2006**, *35*, 199–202. [CrossRef]
29. Heinhold, R.; Williams, G.T.; Cooil, S.P.; Evans, D.A.; Allen, M.W. Influence of polarity and hydroxyl termination on the band bending at ZnO surfaces. *Phys. Rev. B Condens. Matter* **2013**, *88*, 235315. [CrossRef]
30. Chen, M.; Wang, W.; Yu, Y.H.; Pei, Z.I.; Bai, X.D.; Sun, C.; Huang, R.F.; Wen, L.S. X-ray photoelectron spectroscopy and auger electron spectroscopy studies of Al-doped ZnO films. *Appl. Surf. Sci.* **2000**, *158*, 134. [CrossRef]
31. Zhang, X.; Qin, J.; Xue, Y.; Yu, P.; Zhang, B.; Wang, L.; Liu, R. Effect of aspect ratio and surface defects on the photocatalytic activity of ZnO nanorods. *Sci. Rep.* **2014**, *4*, 4596. [CrossRef] [PubMed]
32. Al-Gaashani, R.; Radiman, S.; Daud, A.R.; Tabet, N.; Al-Douri, Y. XPS and optical studies of different morphologies of ZnO nanostructures prepared by microwave methods. *Ceram. Int.* **2013**, *39*, 2283–2292. [CrossRef]
33. Lin, K.F.; Cheng, H.M.; Hsu, H.C.; Hsieh, W.F. Electronic structures, and surface states of ZnO finite well structures. *Appl. Phys. Lett.* **2006**, *88*, 263117. [CrossRef]
34. Cusco, R.; Alarco- Lladó, E.; Ibáñez, J.; Artús, L.; Jiménez, J.; Wang, B.; Callahan, M.J. Temperature dependence of Raman scattering in ZnO. *Phys. Rev. B Condens. Matter.* **2007**, *75*, 165202. [CrossRef]
35. Roy, N.; Chowdhury, A.; Paul, T.; Roy, A. Morphological, Optical, and Raman Characteristics of ZnO Nanoflowers on ZnO-Seeded Si Substrates Synthesized by Chemical Method. *J. Nanosci. Nanotechnol.* **2016**, *16*, 9738–9745. [CrossRef]
36. Suriani, A.B.; Safitri, R.N.; Mohamed, A.; Alfarisa, S.; Isa, I.M.; Kamari, A.; Hashim, N.; Ahmed, M.K.; Malek, M.F.; Rusop, M. Enhanced field electron emission of flower-like zinc oxide on zinc oxide nanorods grown on carbon nanotubes. *Mater. Lett.* **2015**, *149*, 66–69. [CrossRef]
37. Zhang, L.; Zhao, J.; Zheng, J.; Li, L.; Zhu, Z. Shuttle-like ZnO nano/microrods: Facile synthesis, optical characterization and high formaldehyde sensing properties. *Appl. Surf. Sci.* **2011**, *258*, 711–718. [CrossRef]
38. Ghimbeu, C.M.; Schoonman, J.; Lumbreras, M.; Siadat, M. Electrostatic spray deposited zinc oxide films for gas sensor applications. *Appl. Surf. Sci.* **2007**, *253*, 7483–7489. [CrossRef]
39. Nafees, M.; Liaqut, W.; Ali, S.; Shafique, M.A. Synthesis of ZnO/Al: ZnO nanomaterial: Structural and band gap variation in ZnO nanomaterial by Al doping. *Appl. Nanosci.* **2013**, *3*, 49–55. [CrossRef]
40. Anandkumar, M.; Lathe, A.; Palve, A.M.; Deshpande, A.S. Single-phase $Gd_{0.2}La_{0.2}Ce_{0.2}Hf_{0.2}Zr_{0.2}O_2$ and $Gd_{0.2}La_{0.2}Y_{0}{\cdot}_2Hf_{0.2}Zr_{0.2}O_2$ nanoparticles as efficient photocatalysts for the reduction of Cr(VI) and degradation of methylene blue dye. *J. Alloys Compd.* **2021**, *850*, 156716. [CrossRef]
41. Kong, Y.C.; Yu, D.P.; Zhang, B.; Fang, W.; Feng, S.Q. Ultraviolet-emitting ZnO nanowires synthesized by a physical vapor deposition approach. *Appl. Phys. Lett.* **2001**, *78*, 407. [CrossRef]
42. Lin, B.; Fu, Z.; Jia, Y. Green luminescent center in undoped zinc oxide films deposited on silicon substrates. *Appl. Phys. Lett.* **2001**, *79*, 943. [CrossRef]
43. Ahn, H.C.; Kim, Y.Y.; Kim, D.C.; Mohanta, S.K.; Cho, H.K. A comparative analysis of deep level emission in ZnO layers deposited by various methods. *J. Appl. Phys.* **2009**, *105*, 013502. [CrossRef]
44. Antoniadou, M.; Arfanis, M.K.; Ibrahim, I.; Falaras, P. Bifunctional g-C3N4/WO3 thin films for photocatalytic water purification. *Water* **2019**, *11*, 2439. [CrossRef]
45. Xu, Y.; Schoonen, M.A.A. The Absolute Energy Positions of Conduction and Valence Bands of Selected Semiconducting Minerals. *Am. Mineral.* **2000**, *85*, 543–556. [CrossRef]
46. Legrini, O.; Oliveros, E.; Braun, A.M. Photochemical processes for water treatment. *Chem. Rev.* **1993**, *93*, 671–698. [CrossRef]
47. Ozer, L.Y.; Garlisi, C.; Oladipo, H.; Pagliaro, M.; Sharief, S.A.; Yusuf, A.; Almheiri, S.; Palmisano, G. Inorganic semiconductors-graphene composites in photo(electro)catalysis: Synthetic strategies, interaction mechanisms and applications. *J. Photochem. Photobiol. C Photochem. Rev.* **2017**, *33*, 132–164. [CrossRef]

Disclaimer/Publisher's Note: The statements, opinions and data contained in all publications are solely those of the individual author(s) and contributor(s) and not of MDPI and/or the editor(s). MDPI and/or the editor(s) disclaim responsibility for any injury to people or property resulting from any ideas, methods, instructions or products referred to in the content.